CHINESE OPTICS LETTERS

Vol. 19, No. 12 | December 2021

High-performance ultra-compact polarization splitter-rotators based on dual-etching and tapered asymmetrical directional coupler

Changjian Xie (解长健)[1], Xihua Zou (邹喜华)[1*], Fang Zou (邹 放)[1], and Yong Zhang (张 永)[2]

[1] Center for Information Photonics and Communications, School of Information Science and Technology, Southwest Jiaotong University, Chengdu 611756, China

[2] State Key Laboratory of Advanced Optical Communication Systems and Networks, Department of Electronic Engineering, Shanghai Jiao Tong University, Shanghai 200240, China

*Corresponding author: zouxihua@swjtu.edu.cn

Received April 6, 2021 | Accepted May 21, 2021 | Posted Online September 13, 2021

High-performance ultra-compact polarization splitter-rotators (PSRs) are designed and experimentally demonstrated, using dual etching and a tapered asymmetrical directional coupler. First, two novel PSRs are designed with nanowire and subwavelength grating cross-port waveguides and verified in simulations. Then, one of the two PSRs is fabricated. Experiment results reveal that the extinction ratio is higher than 28 dB or 32 dB at 1550 nm for the launched fundamental transverse magnetic or the transverse electric modes, while the corresponding insertion loss and polarization conversion loss are 0.33 dB and 0.18 dB, respectively.

Keywords: polarization splitter and rotator; silicon photonics; asymmetrical directional coupler; dual etching.
DOI: 10.3788/COL202119.121301

1. Introduction

Photonic integrated circuits (PICs) fabricated in the silicon-on-insulator (SOI) platform are essential for massive applications in communications, military, and sensing. Due to its CMOS compatibility and ultra-high index contrast in the SOI platform, the PICs can be fabricated with low cost and compact footprint[1–4]. Polarization splitter-rotators (PSRs) are one of the key components in PICs to overcome the highly polarization-dependent issue brought by the silicon waveguide. Typically, the PSR combines the functions of the polarization beam splitter (PBS) and polarization rotators (PRs)[5], so the incident light with orthogonal polarization can be separated and rotated on one of them. Thus, the PSRs are widely used to meet significant requirements for polarization processing and multiplexing. Recently, various PSRs have been proposed with different structures, such as the mode-sorting asymmetric Y-junction[6,7], multimode interferometer[8,9], and asymmetric directional coupler (ADC)[10–13]. Among them, the PSRs fabricated by the ADC structure have advantages on performance, footprint, and design flexibility. However, this type of PSR is sensitive to fabrication errors. To address this problem, several novel concepts have been incorporated into the ADC structures, such as subwavelength grating (SWG), hybrid plasmonic waveguide, and quasi-adiabatic couplers. A PSR based on the SWG-ADC structure was numerically proposed[14], improving the fabrication tolerance from ±3 nm to ±40 nm for waveguide width. A hybrid plasmonic-dielectric-based PSR is also demonstrated in Ref. [15]. Using this structure, the PSR obtains an ultra-high extinction ratio [ER, more than 58 dB for the transverse magnetic (TM) polarization mode]. However, the hybrid plasmonic is complicated to realize under current commercial tape-out processing conditions. Therefore, a better choice is to use a quasi-adiabatic taper coupler. A PSR comprising a silicon wire waveguide coupled to a taper-etched waveguide is designed[16], such that the partially etched taper can compensate for fabrication errors. The ER reaches 30 dB within a 160 nm bandwidth. Nevertheless, the footprint beyond 200 μm is too large to meet the stringent requirements for compactness.

In this Letter, we design two novel PSRs, and one sample of them is fabricated by using electron-beam lithography (EBL). Both PSRs are dual etched in the through-port waveguide. The first level taper etching is used to meet the phase matching condition, for achieving the high-efficiency cross coupling between the TM_0 mode in the etching region and the transverse electric (TE_0) mode in the other waveguide. Then, after an S bend section, the etched width is gradually increased, and the full etching is formed. In this region, the residual TM_0 mode will leak into the SiO_2 substrate. A reverse taper-etched structure is used at the end of the through port to restore the waveguide

thickness to 220 nm. The cross-port waveguides of two PSRs are SWG and nanowire waveguide. One PSR is fabricated and tested, showing an ER of more than 20 or 28 dB over 1510–1580 nm for TE_0 or TM_0 modes. For a launched TE_0 mode, the insertion loss (IL) is less than 0.6 dB within the 70 nm bandwidth. For a launched TM_0 mode, the polarization conversion loss (PCL) is less than 1 or 3 dB within the bandwidth of 45 or 70 nm, respectively.

2. Design and Principle

The ultra-compact PSRs are designed based on the ADC structure. The top cladding of the PSR is specified as air to achieve a more compact footprint[17]. The schematic diagrams of the two PSRs are shown in Fig. 1. The through-port waveguides of two PSRs are both dual etched. The first stage is partially etched, and a tapered coupler is formed in the coupling region. An S bend section is used to decouple at the end of the coupling region. Meanwhile, the etching width remains unchanged until arriving at the end of the S bend. Then, the etched width is gradually increased, and it finally forms a full etching. Right now, the waveguide supports a single mode, and only the TE_0 mode can be guided in this port. A reverse taper is used to recover the waveguide thickness. The cross-port waveguide might be an SWG or a nanowire, as shown in Figs. 1(a) and 1(b).

For the two PSRs, W_1 is set as 0.628 μm. According to the fabrication process requirements, the etching depth is specified to be 70 nm. Since the cross-port waveguide should be phase matched with the through-port waveguide, the variation of the TE_0 and TM_0 effective refractive indices is investigated, with the etching width in the through-port waveguide. The effective refractive index of the TM_0 mode is between 1.45 and 1.7. Meanwhile, the equivalent material refractive index of the SWG waveguide can be calculated by a simplified model[18],

$$\Delta n_{eq} = \delta \cdot \Delta n, \tag{1}$$

where Δn_{eq} is the refractive index difference between the equivalent material and air cladding, δ is the duty cycle, and Δn is the refractive index difference between the silicon and air cladding. According to this relationship, we first determine $W_3 = 0.522\,\mu m$ in PSR-1, and the end width of taper W_2 is optimized as 0.32 μm to avoid the $TM_0 - TM_0$ coupling between two waveguides. The SWG has a period of 0.3 μm and a duty-cycle of 0.7. With these values, we sweep the coupling length, and the result is shown in Fig. 2. It is clear that the optimal coupling length is 14.8 μm.

For the nanowire waveguide in PSR-2, $W_3 = 0.3\,\mu m$ and $W_2 = 0.36\,\mu m$ are specified. With this condition, we sweep the length of L_c with different gaps, as shown in Fig. 3. The conversion loss reaches the minimum value when $L_c = 6.2\,\mu m$ and $g = 100$ nm.

Figure 4 shows the conversion efficiency at the cross port and the through port of PSR-1 and PSR-2. Clearly, the ER is higher than 15 dB and 25 dB, and the loss is lower than 1 dB and 0.3 dB within the 130 nm and 20 nm bandwidth for PSR-1, respectively. For PSR-2, the obtained ER is higher than 15 dB, 20 dB, or 30 dB, while the loss is lower than 0.4 dB, 0.9 dB, or 1 dB within the bandwidth of 33 nm, 100 nm, or 150 nm, as shown in Figs. 4(c) and 4(d).

To reveal the fabrication tolerance of the two PSRs, we keep the center position constant and synchronously change the waveguide width. The results are shown in Fig. 5. PSR-1 and PSR-2 have ±20 nm or ±10 nm fabrication tolerance, respectively. Compared with PSR-2, PSR-1 based on the SWG waveguide has a larger fabrication tolerance in terms of PCL, but its errors on duty cycle will distort the performance. On the other hand, PSR-2 has better ER performance in a wider bandwidth.

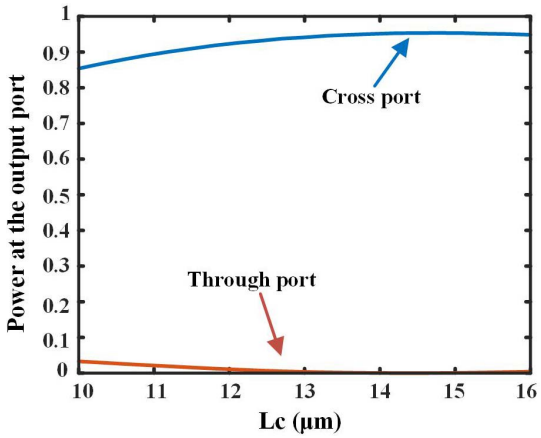

Fig. 2. Coupling efficiency of PSR-1 varies with the L_c.

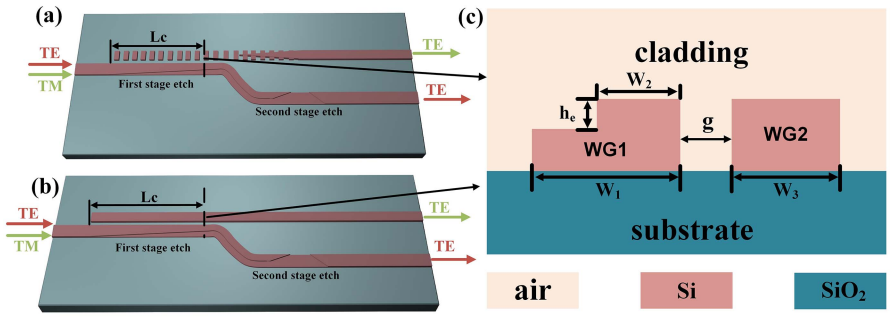

Fig. 1. Schematic diagrams of the two proposed PSRs. (a) PSR-1. (b) PSR-2. (c) Cross view.

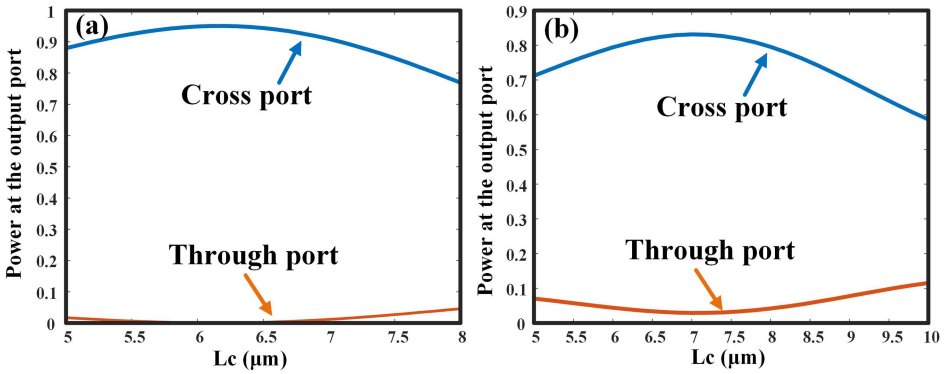

Fig. 3. Output powers from the through and cross ports vary with the length of L_c. (a) $g = 100$ nm, (b) $g = 150$ nm.

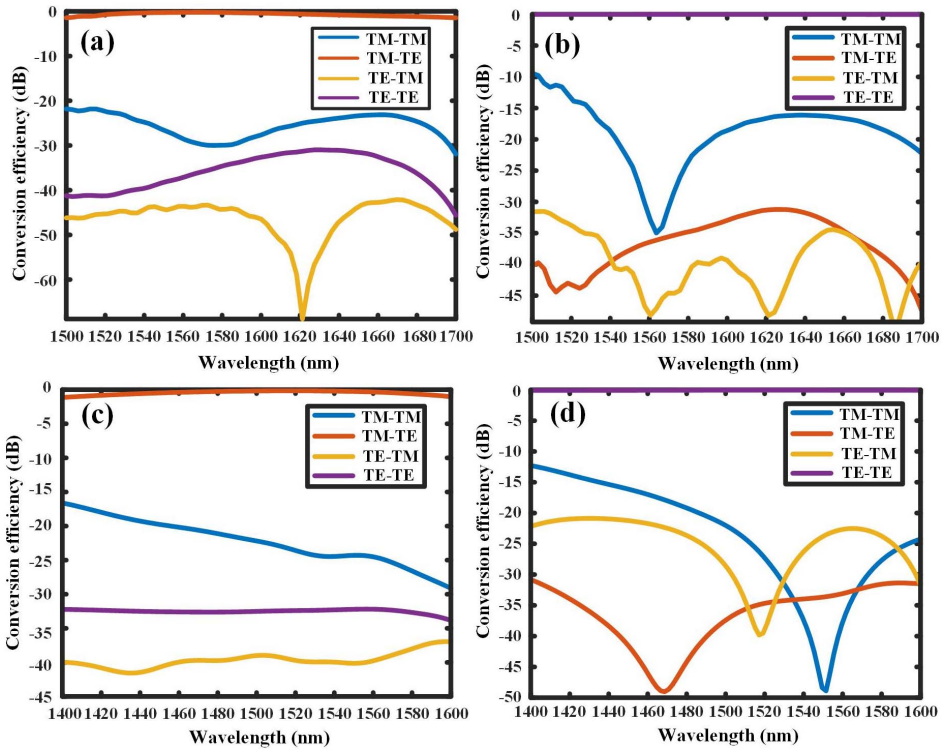

Fig. 4. Conversion efficiency of PSR-1 at the (a) cross port and (b) through port; conversion efficiency of PSR-2 at the (c) cross port and (d) through port.

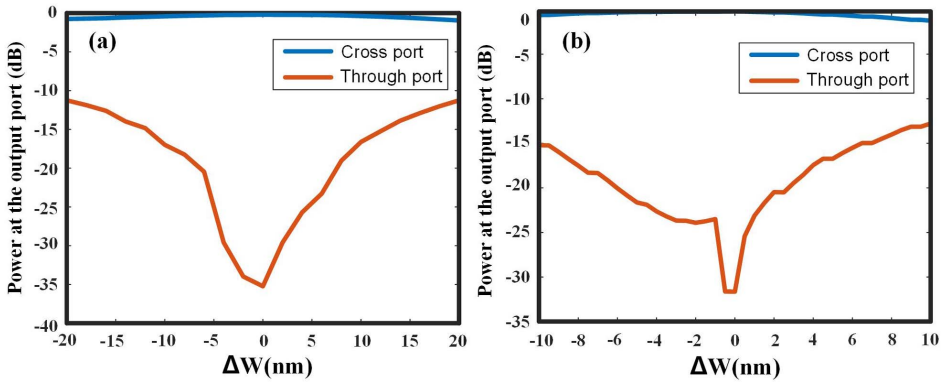

Fig. 5. Fabrication tolerance of (a) PSR-1 and (b) PSR-2.

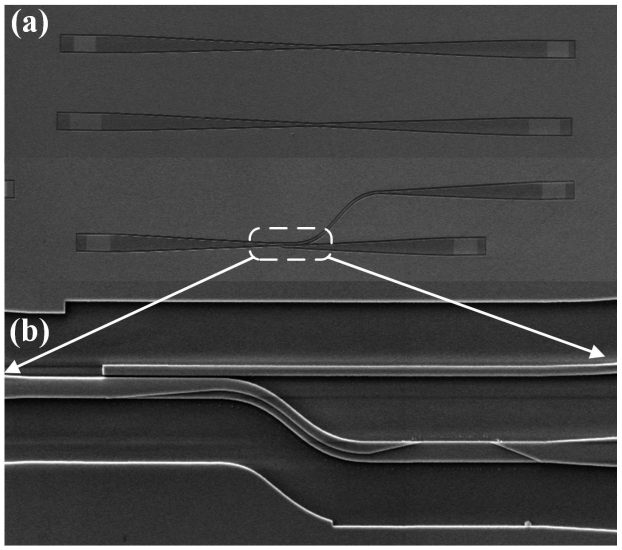

Fig. 6. (a) SEM images of the reference waveguide and PSR. (b) Main structure of the PSR.

3. Fabrication and Measurement

Based on the above analysis, we fabricated the PSR-2 within a 4 mm × 4 mm SOI wafer, which has a 220 nm silicon layer and a 3 μm SiO_2 substrate. The EBL was used to define the patterns of grating couplers on the ZEP520A resist[19]. Then, the patterns were transferred to the top silicon layer by inductively coupled plasma (ICP) dry etching with a 70 nm etching depth, using SF_6 and C_4F_8 gases. Second, the PSR structures were patterned on the wafer by EBL and ICP etching with a full etch depth of 220 nm. The scanning electron microscope (SEM) image of the fabricated PSR samples is shown in Fig. 6.

We designed two vertical coupling gratings for supporting the TE_0 and TM_0 modes, respectively. The period and filling factor of the TE_0 grating coupler are designed as 620 nm and 45%, while 1050 nm and 47% are for the corresponding TM_0 grating coupler. During the performance tests, several TE_0–TE_0 and TM_0–TM_0 reference waveguides are fabricated, and their transmission responses are shown in Fig. 7. It can be found that coupling losses of TE_0 and TM_0 grating couplers are 7.7 dB/port and 11.4 dB/port at the center wavelength, respectively.

The experiment and simulation results for PSRs are shown in Fig. 8, after being calibrated with the reference waveguide. The IL of the TE_0 mode in through port is less than 0.6 dB within the bandwidth of 1510–1580 nm, while the ER is higher than 20 dB. The TM_0–TE_0 conversion efficiency reaches the maximum of 96% at $\lambda = 1550$ nm, with a PCL of 0.18 dB. In the 1535–1580 nm range, the PCL is less than 1 dB, and the ER is larger than 28 dB.

In addition, a comparison among similar PSRs recently reported is listed in Table 1. It is clear that the fabricated

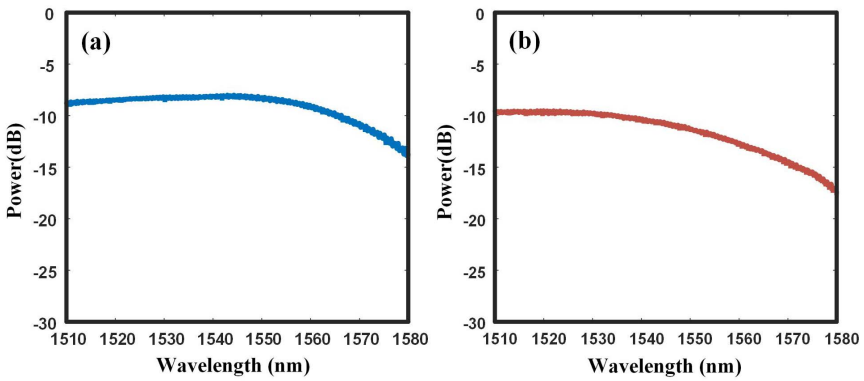

Fig. 7. Transmission response of the (a) TE_0 and (b) TM_0 vertical coupling gratings.

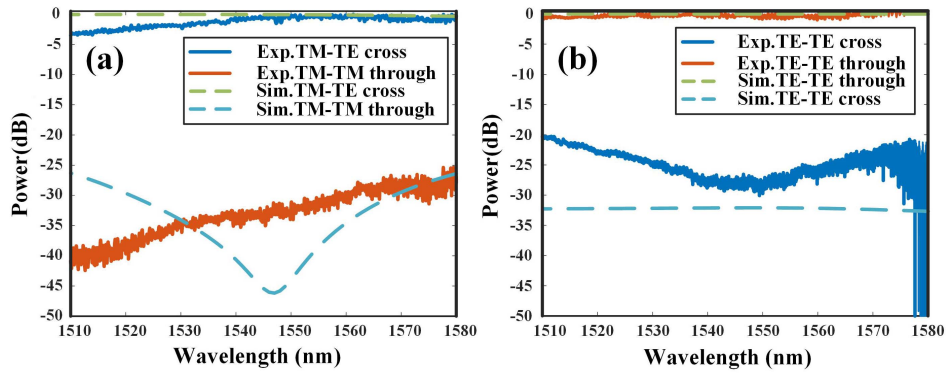

Fig. 8. Transmission spectral responses: (a) TM_0 mode launched and (b) TE_0 mode launched.

Table 1. Performance Comparison among PSRs (Fabricated Samples).

Structure	Footprint (μm)	PCL (dB)	ER (dB)	Bandwidth (nm)	Tolerance (nm)
Sub-wavelength grating coupler and secondary filtering[18]	> 36	< 1	13	73	±50
Sub-wavelength grating coupler[20]	35	0.3	10	50	±3
Discretized subwavelength nanostructure[21]	7.92	1	25	40	±10
Counter-tapered coupler[22]	170	0.8	18	60	±20
Mode-evolution and an asymmetric directional coupler[23]	170	1.5	10	40	±10
This work	28	1	28	45	±10

PSR-2 has excellent comprehensive characteristics in compact footprint, PCL, ER, and bandwidth, particularly the highest ER of 28 dB within the 45 nm bandwidth.

4. Conclusion

We have designed two novel PSRs based on the dual-etched and tapered ADC. The $TM_0 - TE_0$ conversion is fulfilled by taper etching in the coupling region, and the residual TM_0 mode is filtered out by the second stage etching. Using the EBL, PSR-2 is fabricated and tested. Experiment results show a maximum IL of 0.6 dB and a minimum ER of 20 dB within the 70 nm bandwidth for the TE_0 mode. For $TM_0 - TE_0$ conversion, the ER is higher than 28 dB over the 1510–1580 nm range, and the PCL is less than 1 dB within the 45 nm bandwidth.

Acknowledgement

This work was supported by the National Key Research and Development Program of China (No. 2019YFB2203600).

References

1. X. Wang, G. Zhou, Z. Jin, L. Lu, G. Wu, L. Zhou, and J. Chen, "Wavelength-mode pulse interleaver on the silicon photonics platform," Chin. Opt. Lett. **18**, 031301 (2020).
2. Y. Zhang, Y. He, X. Jiang, B. Liu, C. Qiu, Y. Su, and R. A. Soref, "Ultra-compact and highly efficient silicon polarization splitter and rotator," APL Photon. **1**, 091304 (2016).
3. T. Tsuchizawa, K. Yamada, H. Fukuda, T. Watanabe, J.-I. Takahashi, M. Takahashi, T. Shoji, E. Tamechika, S. Itabashi, and H. Morita, "Microphotonics devices based on silicon microfabrication technology," IEEE J. Sel. Top. Quantum Electron. **11**, 232 (2005).
4. W. Bogaerts, R. Baets, P. Dumon, V. Wiaux, S. Beckx, D. Taillaert, B. Luyssaert, J. V. Campenhout, P. Bienstman, and D. V. Thourhout, "Nanophotonic waveguides in silicon-on-insulator fabricated with CMOS technology," J. Lightwave Technol. **23**, 401 (2005).
5. D. Dai, K. Ma, and H. Wu, "Mode/polarization manipulation in silicon photonics," J. Phys. Conf. Series **844**, 012039 (2017).
6. S. Keyvaninia, H. Boerma, M. Wössner, F. Ganzer, P. Runge, and M. Schell, "Highly efficient passive InP polarization rotator-splitter," Opt. Express **27**, 25872 (2019).
7. J. Wang, B. Niu, Z. Sheng, A. Wu, W. Li, X. Wang, S. Zou, M. Qi, and F. Gan, "Novel ultra-broadband polarization splitter-rotator based on mode-evolution tapers and a mode-sorting asymmetric Y-junction," Opt. Express **22**, 13565 (2014).
8. H. Liang, R. Soref, and J. Mu, "Compact polarization splitter based on a silicon angled multimode interferometer structure," Appl. Opt. **58**, 4070 (2019).
9. Y. Ding, H. Ou, and C. Peucheret, "Wideband polarization splitter and rotator with large fabrication tolerance and simple fabrication process," Opt. Lett. **38**, 1227 (2013).
10. B. Bai, L. Pei, J. Zheng, T. Ning, and J. Li, "Ultra-short plasmonic polarization beam splitter-rotator using a bent directional coupler," Chin. Opt. Lett. **18**, 041301 (2020).
11. Z. Ying, G. Wang, X. Zhang, H.-P. Ho, and Y. Huang, "Ultracompact and broadband polarization beam splitter based on polarization-dependent critical guiding condition," Opt. Lett. **40**, 2134 (2015).
12. J. Wang, B. Niu, Z. Sheng, A. Wu, X. Wang, S. Zou, M. Qi, and F. Gan, "Design of a SiO_2 top-cladding and compact polarization splitter-rotator based on a rib directional coupler," Opt. Express **22**, 4137 (2014).
13. L. Liu, Y. Ding, K. Yvind, and J. M. Hvam, "Silicon-on-insulator polarization splitting and rotating device for polarization diversity circuits," Opt. Express **19**, 12646 (2011).
14. Y. Xiong, J. G. Wangüemert-Pérez, D.-X. Xu, J. H. Schmid, P. Cheben, and W. N. Ye, "Polarization splitter and rotator with subwavelength grating for enhanced fabrication tolerance," Opt. Lett. **39**, 6931 (2014).
15. B. Bai, L. Liu, and Z. Zhou, "Ultracompact, high extinction ratio polarization beam splitter-rotator based on hybrid plasmonic-dielectric directional coupling," Opt. Lett. **42**, 4752 (2017).
16. Y. Xiong, D.-X. Xu, J. H. Schmid, P. Cheben, S. Janz, and W. N. Ye, "Fabrication tolerant and broadband polarization splitter and rotator based on a taper-etched directional coupler," Opt. Express **22**, 17458 (2014).
17. C. Xie, X. Zou, P. Li, L. Yan, and W. Pan, "Ultracompact silicon polarization splitter-rotator using a dual-etched and tapered coupler," Appl. Opt. **59**, 9540 (2020).
18. Y. He, Y. Zhang, X. Wang, B. Liu, X. Jiang, C. Qiu, Y. Su, and R. Soref, "Silicon polarization splitter and rotator using a subwavelength grating based directional coupler," in *Optical Fiber Communication Conference* (2017), paper Th1G.6.
19. Y. Zhang, Y. He, H. Wang, L. Sun, and Y. Su, "Ultra-broadband mode size converter using on-chip metamaterial-based Luneburg lens," ACS Photon. **8**, 202 (2021).
20. Y. Wang, M. Ma, H. Yun, Z. Lu, X. Wang, N. A. F. Jaeger, and L. Chrostowski, "Ultra-compact sub-wavelength grating polarization splitter-rotator for silicon-on-insulator platform," IEEE Photon. J. **8**, 7805709 (2016).
21. Y. Liu, S. Wang, Y. Wang, W. Liu, H. Xie, Y. Yao, Q. Song, X. Zhang, Y. Yu, and K. Xu, "Subwavelength polarization splitter-rotator with ultra-compact footprint," Opt. Lett. **44**, 4495 (2019).
22. K. Yu, L. Wang, W. Wu, Y. Luo, and Y. Yu, "Demonstration of an on-chip broadband polarization splitter and rotator using counter-tapered coupler," Opt. Commun. **431**, 58 (2019).
23. C. Yuan, J. Dai, H. Jia, J. Ding, L. Zhang, X. Fu, and L. Yang, "Design of a C-band polarization rotator-splitter based on a mode-evolution structure and an asymmetric directional coupler," J. Semicond. **39**, 124008 (2018).